A four-dimensional deconvolution method to correct NA38 experimental data

M C. Abreu, J. Astruc, C. Baglin, A. Baldit, M. Bedjidian, P. Bordalo, A. Borhani, A. Bussiere, J. Castor, T. Chambon, et al.

Institut
de Physique
Nucléaire
de Lyon

Université Claude Bernard

IN2P3 - CNRS

LYCEN 9747

October 1997

A 4-dimensional deconvolution method to correct NA38 experimental data

NA 38 Collaboration

M.C Abreu, M. Bedjidian, D. Contardo, E. Descroix, O. Drapier,
J.Y. Grossiord, A. Guichard, R. Mandry, F. Ohlsson-Malek,
J.R. Pizzi, et al.

A 4-dimensional deconvolution method to correct NA38 experimental data

NA38 Collaboration

M.C. Abreu[a,1], J. Astruc[b], C. Baglin[c], A. Baldit[d],
M. Bedjidian[e], P. Bordalo[a,2], A. Borhani[f], A. Bussière[c],
J. Castor[d], T. Chambon[d], B. Chaurand[f], I. Chevrot[d],
D. Contardo[e], E. Descroix[e,3], A. Devaux[d], O. Drapier[e],
B. Espagnon[d], J. Fargeix[d], R. Ferreira[a,4], F. Fleuret[f],
P. Force[d], J. Gago[a], C. Gerschel[b], M. Gonin[f],
P. Gorodetzky[g,5], J.Y. Grossiord[e], A. Guichard[e,8],
J. Guimarães[a,6], J.P. Guillaud[c], R. Haroutunian[e], D. Jouan[b],
L. Kluberg[f], R. Kossakowski[c], G. Landaud[d], D. Lazic[g],
P. Liaud[c], C. Lourenço[a,4], L. Luquin[d,7], R. Mandry[e],
S. Mourgues[d], F. Ohlsson-Malek[e], S. Papillon[b], P. Petiau[f],
J.R. Pizzi[e], C. Racca[g], S. Ramos[a,2]. A. Romana[f],
B. Ronceux[c], P. Saturnini[d], S. Silva[a], P. Sonderegger[h],
X. Tarrago[b], J. Varela[a,4]

[a] *LIP, Av. E. Garcia, 14-1, P-1000 Lisbon, Portugal*

[b] *Institut de Physique Nucléaire, IN2P3-CNRS et Université de Paris-Sud, F-91406 Orsay Cedex, France*

[c] *Laboratoire d'Annecy-le-Vieux de Physique des Particules, IN2P3-CNRS, B.P. 110, F-74941 Annecy-le-Vieux Cedex, France*

[d] *Laboratoire de Physique Corpusculaire de Clermont-Ferrand IN2P3-CNRS et Université Blaise Pascal, F-63177 Aubière Cedex, France*

[e] *Institut de Physique Nucléaire de Lyon IN2P3-CNRS et Université Claude Bernard, 43, B^d. du 11 Novembre 1918, F-69622 Villeurbanne cedex, France.*

[f] *Laboratoire de Physique Nucléaire des Hautes Energies, Ecole Polytechnique, IN2P3-CNRS, F - 91128 Palaiseau Cedex, France*

[g] *Institut de Recherches Subatomiques, IN2P3-CNRS et Université Louis Pasteur, BP 28, F-67037 Strasbourg Cedex 2, France*

[h] *CERN, CH-1211 Geneva 23, Switzerland*

A four-dimensional method to unfold NA38 experimental distributions is presented. It is based on the Bayes theorem and uses an iterative procedure. Tests of this method on Monte-Carlo simulated distributions are described. Subtraction of the background is discussed. This method is applied to the S-U data collected in 1992 by the NA38 experiment.

1 Introduction

As is well known, the physical distributions studied in many experiments cannot be directly inferred from the measured ones, due to various detector effects such as acceptance and resolution. This is true for the NA38 experiment devoted to the study of dimuon production in heavy ion interactions at the CERN SPS [1]. Physical ($\Phi(x)$) and measured ($I(x')$) quantities are related by the following equation:

$$I(x') = \int S(x'|x)A(x)\Phi(x)dx \qquad (1)$$

where x', x are the sets of kinematical variables associated to the dimuon. $A(x)$ is the acceptance of the detector and $S(x'|x)$ the smearing function giving the probability that a dimuon generated with values x is reconstructed with values x'. These acceptance and smearing functions are calculated via a Monte-Carlo method with a program describing the experimental apparatus.

Up to now, only one-dimensional versions of equation (1) have been used in our data analysis. Two methods have been studied. The first one [2] postulates some analytical representation of the source function $\Phi(x)$ whose parameters are fitted after convolution with the transfer function $S(x'|x)A(x)$ to the experimental distributions. The second method [3] evaluates (using a Monte-Carlo simulation) the unfolding matrix $D(x|x')$ which gives the probability that an event measured with the value x' has been generated with the value x. Such a matrix applied to the data leads to events accepted by the detector from which the physical distributions can be obtained. Note that the

---

[1] Also at FCUL, Universidade de Lisboa, Lisbon, Portugal

[2] Also at IST, Universidade Técnica de Lisboa, Lisbon, Portugal

[3] Now at Université Jean Monnet, Saint-Etienne, France

[4] Now at CERN, Geneva, Switzerland

[5] Now at PPC, Collège de France, Paris, France

[6] Now at Johns Hopkins University, Baltimore, USA

[7] Now at SUBATECH, Ecole des Mines de Nantes, Nantes, France

[8] Corresponding author

2

matrix D depends on the choice of generation functions used. Both methods rely on the hypothesis that the different kinematical distributions describing the physical processes are separable. For a given process, the acceptance of the apparatus in one of the variables does not depend on this variable distribution itself. However, it is a function of the shape of the other kinematical variable distributions needed to describe the process. This implies knowing the distributions which we want to extract from the data. In addition, these methods do not take into account possible correlations among the variables. To avoid these difficulties related to the one-dimensional unfolding methods, one has to consider multi-dimensional methods. The purpose of this paper is to describe one of these methods. We first discuss the procedure chosen for evaluating acceptance and smearing matrices. The deconvolution technique based on the Richardson-Lucy algorithm [4,5] is presented together with tests of the method. Finally, this unfolding procedure is applied to the S-U data collected in 1992.

2 Set-up description and dimuon kinematical variables

The NA38 set-up consists of beam counters, an active segmented target, an electromagnetic calorimeter used to estimate the centrality of the interaction, and a muon spectrometer [6]. The muon spectrometer (Fig. 1) is composed of a beam dump surrounded by a hadron absorber, an air-core toroidal magnet of hexagonal symmetry, two sets of four multiwire proportional chambers (MWPC) and six hodoscopes of plastic scintillator, four of them (R1, R2, R3 and R4) providing the trigger. Hodoscopes and MWPC also exhibit an hexagonal symmetry and a dimuon trigger occurs when two muons are detected in two different sextants. Opposite-sign ($\mu^+\mu^-$) as well as like-sign ($\mu^+\mu^+$ and $\mu^-\mu^-$) muon pairs are recorded, as the background contribution to the opposite-sign spectra can be deduced from the like-sign pair distributions (see section 6).

The signal dimuon quadrivector ($E_{\mu\mu}, \overrightarrow{P}_{\mu\mu}$), sum of two opposite-sign muon quadrivectors, depends upon 8 variables. Taking into account the muon mass reduces this number to six. Assuming rotation invariance, we are left with 5 variables. The following list of the dimuon kinematical variables has been considered: mass M, transverse momentum P_T, rapidity y_{cm} in the center of mass frame, polar and azimuthal angles θ_{cs} and φ_{cs} in the Collins-Soper system [7]. Since we cannot infer the nucleon-nucleon reaction plane (needed for φ_{cs} determination) from the measured quantities, we restrict ourselves to four useful variables and we will consider a four-dimensional unfolding of the data with the M, P_T, y_{cm} and $\cos\theta_{cs}$ variables. Acceptance and smearing functions will not depend on the shape of the distributions of these four variables.
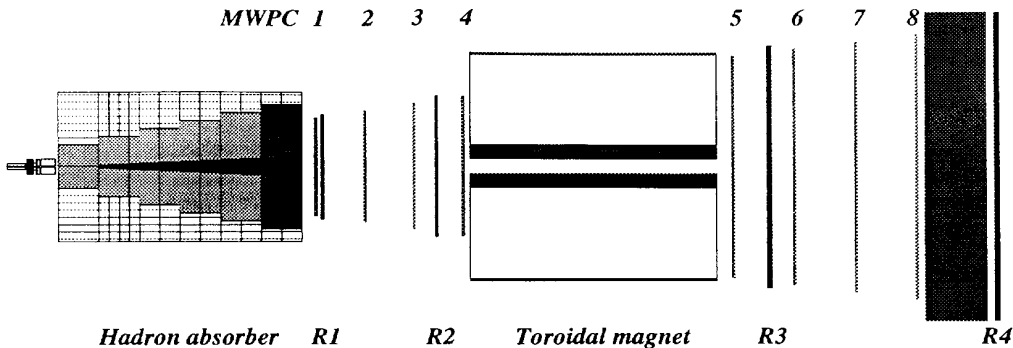
3

Fig. 1. Overview of the NA38 spectrometer.

3 Acceptance and smearing matrices

As we are dealing with histogram data, Eq. (1) has to be discretized and the acceptance and smearing continuous functions will be evaluated in a matrix form. These matrices are computed using the NA38 detector simulation programs [8] (Dimujet/Dimurec) as explained below. We define in Table 1 the ranges of the four dimuon variables considered.

Table 1
Range of the dimuon kinematical variables.

Variable	Minimum	Maximum	Step	Nb. channels
$M(\mathrm{GeV}/c^2)$	1	8	0.1	70
$P_T(\mathrm{GeV}/c)$	0	5	0.1	50
y_{cm}	-0.3	1.2	0.05	30
$\cos \theta_{cs}$	-0.8	0.8	0.05	32

3.1 Acceptance calculation

The grid defined in Table 1 contains $3.36 \ 10^6$ cells. We restrict the acceptance calculation to $M > 1.4$ GeV/c^2, $0 < y_{cm} < 1$ and $|\cos \theta_{cs}| < 0.5$, in order to avoid smearing edge effects. This subspace corresponds to $1.12 \ 10^6$ cells. As the acceptance calculation for each cell would be extremely time-consuming, we calculate a reduced set of acceptance points with Dimujet/Dimurec and interpolate for the other nodes of the grid, in the regions where the acceptance changes slowly. In practice, we evaluate the acceptance for 16 nodes (over 70) for M, and 22 nodes (over 50) for P_T, and all the y_{cm} and positive $\cos \theta_{cs}$ nodes (as the acceptance is symmetrical with respect to $\cos \theta_{cs}$). In summary,

4

the computed nodes are those given in Table 2.

Table 2
List of the nodes for which the acceptance has been calculated.

M	1.45	1.55	1.75	2.05	2.55	3.05	3.55	4.05		
(GeV/c^2)	4.55	5.05	5.55	6.05	6.55	7.05	7.55	7.95		
P_T	0.05	0.15	0.25	0.35	0.45	0.55	0.65	0.75	0.85	0.95	1.05
(GeV/c)	1.25	1.45	1.65	1.85	2.05	2.25	2.75	3.25	3.75	4.35	4.95
y_{cm}	0.025	0.075	0.125	0.175	0.225	0.275	0.325	0.375	0.425	0.475	
	0.525	0.575	0.625	0.675	0.725	0.775	0.825	0.875	0.925	0.975	
$\cos\theta_{cs}$	0.025	0.075	0.125	0.175	0.225	0.275	0.325	0.375	0.425	0.475	

This results in an array of $70.4 \, 10^3$ elements which can be easily stored. Interpolation for acceptance calculations is done in the (M, P_T) subspace using the CERNLIB program DIVDIF [9].

3.2 Smearing matrix evaluation

The smearing matrix depends upon 8 variables leading to $\sim 10^{13}$ elements to be computed and stored, which is presently impossible. In addition, a direct call to the simulation/reconstruction programs is not possible due to the large amount of time needed to compute the 4-d smearing matrix for each dimuon. We therefore evaluate the dimuon smearing from the single muon smearing, which was determined using the simulation programs.

The procedure is the following: for a dimuon generated with $(M, P_T, y_{cm}, \cos\theta_{cs})$, the momentum components (p_x, p_y, p_z) of each of the muons is obtained taking the nucleon Fermi motion in each nucleus randomly from distributions of ref. [10]. The azimuthal angles in the nucleon-nucleon center of mass (φ_{cm}) and in the Collins-Soper frame (φ_{cs}) are uniformly distributed and the sign of the first muon is also taken randomly. The position of the interaction subtarget (one out of the 10 subtargets used in the S-U setup) is sampled uniformly within the target region. In order to describe the smearing of the single muons due to multiple scattering in the absorber and to the precision on the momentum measurement, one has to find uncorrelated distributions of the kinematical variables. Simulation studies lead to the following uncorrelated variables:

$$P_T \Delta\varphi \qquad \text{with} \qquad \Delta\varphi = \varphi' - \varphi \qquad (2)$$
$$P\Delta\theta = f(P) \qquad \text{with} \qquad \Delta\theta = \theta' - \theta \qquad (3)$$

5

$$\frac{\Delta P}{P} * \left(\frac{1}{P_T + \frac{0.3}{P_T}} \right) = f(P) \qquad \text{with} \qquad \Delta P = P' - P \qquad (4)$$

for 10 bins in polar angle θ where P, P_T, θ and φ are respectively the generated total momentum, transverse momentum, polar and azimuthal angles of the single muon, and P', θ', φ' refer to the reconstructed values. The distribution (4) depends slightly on the polar angle θ and has been computed for 10 values of θ. The distributions (2-4) are shown in Fig. 2 for the NA38 experiment corresponding to the 1992 S-U set-up at 200 GeV/c per incident nucleon.
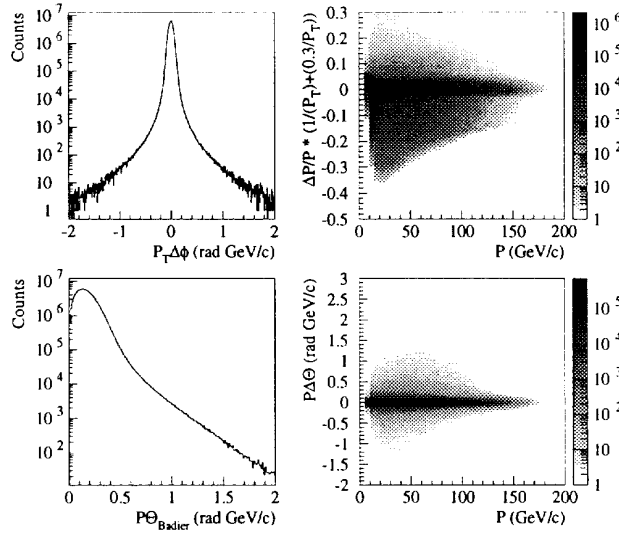

Fig. 2. Distributions of the muon smearing functions.

From the sampling of these distributions, we can deduce the smeared values p'_x, p'_y, p'_z of each of the muons. One has then to check that the smeared muons go through the spectrometer and fulfill the trigger requirements. This implies the sampling of two other distributions which connect the estimated track from the Badier plane [11] to the measured one after the absorber given by the four multiwire chambers before the magnet (see Fig. 3). The simulation program shows that the polar angle θ_{Badier} between the two tracks can be determined by sampling the $P\theta_{Badier}$ distribution (see Fig. 2), which does not depend on the other kinematical variables of the muon, and that the azimuthal angle φ_{Badier} can be generated isotropically. From these angles, the track position on the first four multiwire chambers and on the two scintillator hodoscopes R1 and R2 is computed. The track coordinates are then compared to the geometrical limits of the different detectors. Then, the trigger condition based on R1 and R2 is checked (a coincidence of slats from R1 and R2, $R1_i*R2_i$ or $R1_i*R2_{i-1}$, is required in order to select tracks from the target region). For muons which survive these requirements, the deviation angle $\Delta\alpha$ due to the

6

toroidal magnetic field is computed via a first order formula: $\Delta\alpha = \frac{k}{P_T}$ [6]. The hit positions in the backward telescope (4 MWPC, R3 and R4) can be deduced and checked against the different geometrical dimensions. Depending on the slat number i of the R1*R2 coincidence, the trigger requires a range of slats in R3 and R4, and such a condition is checked for each of the muons. In order to ensure the same acceptance for μ^+ and μ^-, an additional condition ("image cut") is required: for a muon of a given charge, the muon with the opposite charge and the same kinematical variables has to be accepted in the apparatus. If all these requirements are fulfilled for both muons, and if the two muons are in different sextants, then the kinematical variables $(M', P'_T, y'_{cm}, \cos\theta'_{cs})$ of the smeared dimuon can be calculated. The whole process, starting from the sampling of the Fermi motion distributions, is repeated several times (more details below) to compute the 4-dimensional smearing sub-matrix for the dimuon generated with $(M, P_T, y_{cm}, \cos\theta_{cs})$.

A comparison of the smearing obtained with this method and the one calculated with the Monte-Carlo simulation program is shown in Fig. 4 for each projection.

One can see that the agreement of the method described here with the standard simulation is quite good. This agreement has been checked for several nodes (≈ 50), including non central ones. In addition this method is faster (by a factor of ~ 50) than the simulation/reconstruction programs.
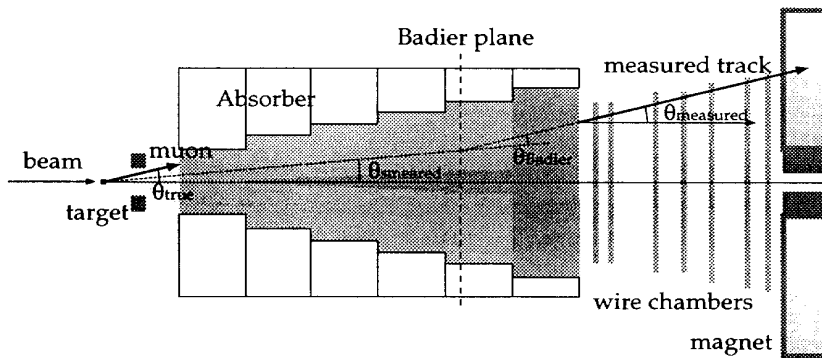

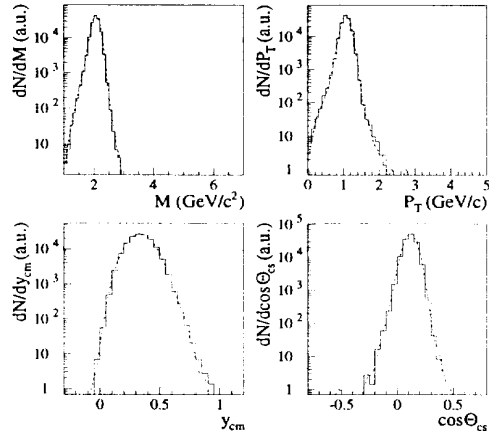Fig. 3. Extrapolation of the measured track to the Badier plane.

7

Fig. 4. Comparison between dimuon smearing calculated from single muons (solid lines) and simulated by Monte-Carlo programs (dashed lines), for a given node ($M = 2.05$ GeV/c^2, $P_T = 1.05$ GeV/c, $y_{cm} = 0.325$, $\cos \theta_{cs} = 0.125$).

4 The Richardson-Lucy method

We are going to use the method proposed independently by Richardson [4] and Lucy [5] to solve Eq. (1). It is based on the Bayes theorem. Let $P(A|B)$ be the probability that A is true given that B is, and $P(A)$ and $P(B)$ to be the unconditional probabilities. The Bayes formula states that

$$P(A|B) = P(A)\frac{P(B|A)}{P(B)}$$

Let us write Eq. (1) as:

$$I(x') = \int S(x'|x)O(x)dx \qquad \text{with} \qquad O(x) = A(x)\Phi(x)$$

One can write

$$O(x) = \int Q(x|x')I(x')dx'$$

where $Q(x|x')$ can be related to $S(x'|x)$ via Bayes theorem:

$$Q(x|x') = O(x)\frac{S(x'|x)}{I(x')}$$

$Q(x|x')$ in turn depends on the knowledge of $O(x)$, which we are looking for. To solve this problem, $Q(x|x')$ is calculated using an iteration approach:

$$Q^n(x|x') = O^n(x)\frac{S(x'|x)}{I^n(x')}$$

and

$$O^n(x) = \int Q^{n-1}(x|x')I^0(x')dx' = \int O^{n-1}(x)\frac{S(x'|x)}{I^{n-1}(x')}I^0(x')dx'$$

with $I^0(x')$ being the measured data $D(x')$ and

$$I^{n-1}(x') = \int S(x'|x)O^{n-1}(x)dx$$

In a discrete form:

$$O^n(j) = O^{n-1}(j)\sum_{i=1}^{k} S(i|j)\frac{D(i)}{I^{n-1}(i)} \tag{5}$$

This iterative method forces the deconvoluted spectra to be non-negative. In addition, it conserves the norm at each iteration:

$$\sum_{j=1}^{k} O^n(j) = \sum_{i=1}^{k} D(i) \qquad \forall n$$

9

Moreover, the Richardson-Lucy iteration converges to the maximum likelihood solution for Poisson statistics in the data. Let us remark that this procedure is non-linear.

A choice has to be made in formula (5) for the initial value $O^0(j)$. In principle, any function can be choosen as a starting point. However, in order to speed-up the convergence of the procedure, we take the measured data as the starting distribution. A program based on this method and using the techniques outlined in the previous paragraph for the multidimensional evaluation of acceptance and smearing matrices has been written. Similar deconvolution techniques can be found in [12].

5 Unfolding of test distributions

The accepted source distribution $O^n(j)$ is calculated in the kinematical ranges defined in Table 1. Due to low values of acceptance and smearing edge effects as stressed above, we restrict the calculation of the source distribution to the following intervals:

$$1.4 \leq \quad M \quad < 8 \qquad \text{GeV/c}^2$$

$$0 \leq \quad P_T \quad < 5 \qquad \text{GeV/c}$$

$$0.2 \leq \quad y_{cm} \quad < 0.8$$

$$-0.3 \leq \cos \theta_{cs} < 0.3$$

These cuts remove 30% of the events from the total data sample. Furthermore, cells with acceptance lower than 1% are not taken into account. As the maximum acceptance is about 65%, this cut does not affect significantly the overall normalisation and avoids amplifying by a huge factor cells with negligible content.

To evaluate the deconvolution method, we have generated and reconstructed dimuons arising from a superposition of several mechanisms: Drell-Yan (DY), J/ψ and ψ' with the following distributions [2,3]:

Table 3
Shape of the generated distributions for the different reaction mechanisms.

	M	P_T	y_{cm}	$\cos \theta_{cs}$
DY	$\frac{1}{M^3} \exp - \frac{M}{1.0}$	$P_T \exp - \left(\frac{P_T}{0.71}\right)^{1.4}$	$\exp - \frac{y_{cm}^2}{2*0.76^2}$	$1 + \cos^2 \theta_{cs}$
J/ψ	3.097 GeV/c^2	$P_T \exp - \left(\frac{P_T}{1.14}\right)^{1.7}$	$\exp - \frac{y_{cm}^2}{2*0.57^2}$	uniform
ψ'	3.685 GeV/c^2	$P_T \exp - \left(\frac{P_T}{1.215}\right)^{1.7}$	$\exp - \frac{y_{cm}^2}{2*0.57^2}$	uniform

10

The number of reconstructed dimuons per cell chosen to evaluate the smearing depends upon the mass region. This allows to improve the mass resolution in the J/ψ and ψ' regions without increasing too much the computing time. For $M < 2.8$ GeV/c^2, $2.8 \leq M < 3.4$ GeV/c^2 and $M \geq 3.4$ GeV/c^2, 1000, 5000 and 10000 reconstructed dimuons have been used, respectively.

Unfolding this test distribution with 50 iterations, enough to ensure proper convergence (see Paragraph 7.1), leads to a deconvoluted mass spectrum in which fluctuations appear for $M < 2.8$ GeV/c^2. In order to get rid of this noise, we have to use a different number of iterations, depending on the mass region: 10 for $M < 2.8$ GeV/c^2 and 50 for $M \geq 2.8$ GeV/c^2. This is done by fixing $O^n(j) = O^{10}(j)$ for $n \geq 10$ in the corresponding mass region. The unfolded distributions in the four variables are compared to the generated ones in Fig. 5(a,b) after 50 iterations, and show an overall good agreement. They have been in turn multiplied by the acceptance and smearing matrices and then compared to the reconstructed starting distributions. The agreement is good, as can be seen in Fig. 5(c,d).

One can see, on the mass distribution, that the initial width of the J/ψ and ψ' resonances is not fully restored. In addition, the deconvolution procedure underestimates the continuum in the resonance tails. This so called "Gibbs ring" effect [13] is due to the method itself. Indeed, the factor relating $O^{n-1}(j)$ to $O^n(j)$ in formula (5) depends on the ratio between data and smeared data which is lower than one in the tails of the peaks. We have checked that such an effect does not affect the normalisation of the resonances, as long as the final mass resolution is good enough. The fit of the unfolded mass distribution is displayed on Fig. 6.

In order to take into account the underestimation of the continuum due to the Gibbs rings, the fit has been performed after removal of four points located on both sides of the J/ψ. The histogram channels for $M > 4$ GeV/c^2 have been regrouped in larger width bins. Such a fit allows to subtract the amount of continuum under J/ψ and ψ' resonances in order to extract their P_T distributions. The analysis of the mass and transverse momentum unfolded distributions leads to values of the parameters which are compared to the generated ones in Tables 4 and 5. A satisfactory agreement between unfolded and generated parameters is obtained. Note, however, that the unfolded J/ψ peak position is far from the generated one. This effect is related to a systematic error of the deconvolution method itself and does not affect the peak normalisation. this remark is also true to a lesser extent for the ψ' position. We have also checked that if we introduce a correlation between the variables M and P_T, the deconvolution process is able to reproduce it. Furthermore, it does not create any spurious correlation.
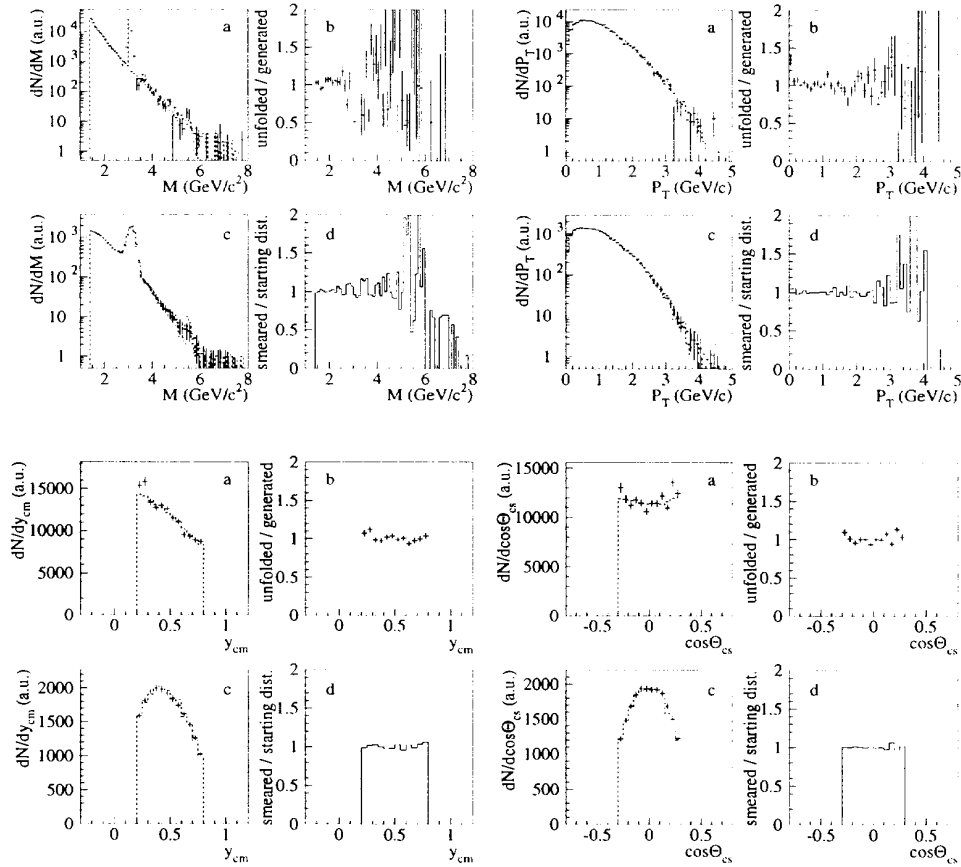
11

Fig. 5. Comparison (a) between unfolded (points) and Monte-Carlo generated distributions (dashed lines) together with their ratio (b). The distribution obtained by smearing the (unfolded) source mass spectrum is compared in (c) with the reconstructed starting distribution. Their ratio is shown in (d).

6 Treatment of background

6.1 Combinatorial background calculation

In addition to signal dimuons, the data include background $\mu^+\mu^-$ pairs originating from uncorrelated π and K decays. In one-dimensional deconvolution methods, this background is evaluated from the recorded like-sign pairs ($\mu^+\mu^+$ and $\mu^-\mu^-$). Assuming that the probabililty to detect a muon of any sign is independent of the sign of the second one and that the multiplicity distributions obey a Poisson law, the number of background events is given by $2\sqrt{N^{++}N^{--}}$, where N^{++} and N^{--} are the numbers of $\mu^+\mu^+$ and $\mu^-\mu^-$, respectively. Such a procedure cannot be applied in a multi-dimensional method, where the cell
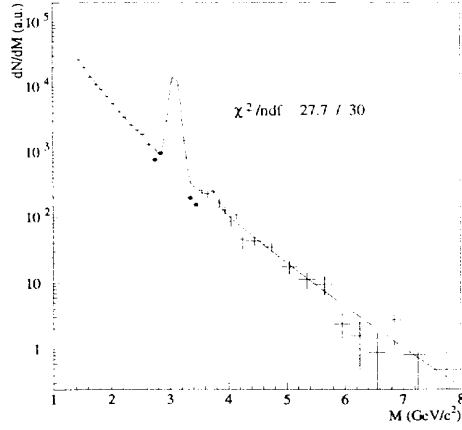
12

Fig. 6. Fit of the unfolded mass distribution (black dots correspond to points removed from the fit).

Table 4

Comparison between generated and unfolded mass distributions.

	Generated	Unfolded
DY Norm	113169	115449±4288
J/ψ Norm	26418	26577±372
ψ' Norm	195	169±66
J/ψ Width (MeV/c^2)	0	71±2
J/ψ Position (GeV/c^2)	3.097	3.087±0.002
ψ' Position (GeV/c^2)	3.685	3.75±0.05
DY Slope (GeV/c^2)	1.00	1.02±0.03

Table 5

Comparison between generated and unfolded P_T distribution moments: $< P_T >$ (GeV/c) and $< P_T^2 >$ (GeV/c)^2.

	Generated		Unfolded	
P_T	$< P_T >$	$< P_T^2 >$	$< P_T >$	$< P_T^2 >$
$2.1 \leq M \leq 2.7$ GeV/c^2	0.86	1.00	0.86 ± 0.02	1.00 ± 0.03
J/ψ	1.14	1.69	1.12 ± 0.02	1.64 ± 0.04
ψ'	1.21	1.92	1.15 ± 0.36	2.00 ± 0.65
$M > 4.2$ GeV/c^2	0.86	1.00	0.91 ± 0.10	1.14 ± 0.16

13

content is frequently zero for N^{++} or N^{--} (or both). To overcome this difficulty, we use a method [14] which calculates the background by means of combinations between all the μ^+ and μ^- distributions from like-sign events. The calculated integrated $\mu^+\mu^-$ background is normalized to $2\sqrt{N^{++}N^{--}}$ with N^{++} and N^{--} being the total numbers of $\mu^+\mu^+$ and $\mu^-\mu^-$ recorded events. The combinatorial background is evaluated for each subtarget and each centrality bin as determined by the transverse energy released in the collision, measured by the electromagnetic calorimeter. The 4-dimensional background $\mu^+\mu^-$ is then subtracted from the 4-dimensional $\mu^+\mu^-$ data. However, in the subtraction process, it may happen that a background cell is filled whereas the corresponding data cell is empty. In this situation, we look for a nearby filled data cell and use it to subtract the background. If the background to be subtracted is larger than the data content of that cell, only the part of the background equal to the cell content is subtracted and the background in excess is in turn reported to the next closest filled data cell. This procedure is repeated until all the background content of the cell is subtracted. In this way, cell contents are always positive or null, never negative. A comparison of background with and without count redistribution is shown in Fig. 7, indicating that this procedure leaves the kinematical distributions of the background unchanged.
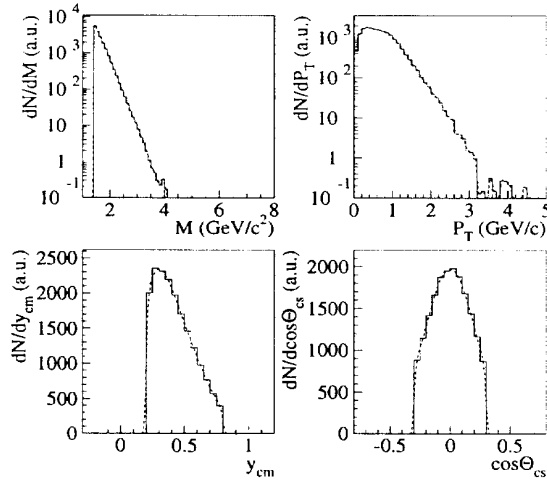

Fig. 7. Comparison between redistributed (solid lines) and non redistributed (dashed lines) background.

6.2 Subtraction of a test background distribution

A trial background has been built as described hereafter. Instead of computing the background with some generator, we consider biparametric spectra $(P_{tot}, \tan\theta)$ of single μ^+ and μ^- extracted from the like-sign muon pairs of the

S-U data, where P_{tot} and $\tan\theta$ are the total momentum and polar angle of the muon. After sampling these distributions and tracking the muons through the apparatus, the corresponding $\mu^+\mu^+$ and $\mu^-\mu^-$ distributions are compared to the experimental ones. If they do not agree, the initial bi-parametric spectra $(P_{tot}, \tan\theta)$ are weighted by the ratio $\frac{\text{data}(P_{tot},\tan\theta)}{\text{reconstructed}(P_{tot},\tan\theta)}$ and this procedure is repeated until the simulated $\mu^+\mu^+$ and $\mu^-\mu^-$ distributions agree with the data. The ratio between positive and negative muons is also verified against the experimental ratio N^{++}/N^{--}. It is then possible to get the simulated background for $\mu^+\mu^+$, $\mu^-\mu^-$ and $\mu^+\mu^-$ pairs. The opposite-sign pairs are then added to the data set of section 5, giving the signal+background test distribution. From the corresponding $\mu^+\mu^+$ and $\mu^-\mu^-$ pairs, the combinatorial background is calculated and subtracted from the signal+background events following the procedure outlined above. Finally, the resulting distribution is unfolded in the same way as presented earlier. The mass projection of the deconvoluted 4-d distributions is presented in Fig. 8 and compared to the test one. Again, the agreement is satisfactory. Similar comparisons (not shown here) have been done for the other variables, leading to an agreement of the same quality.
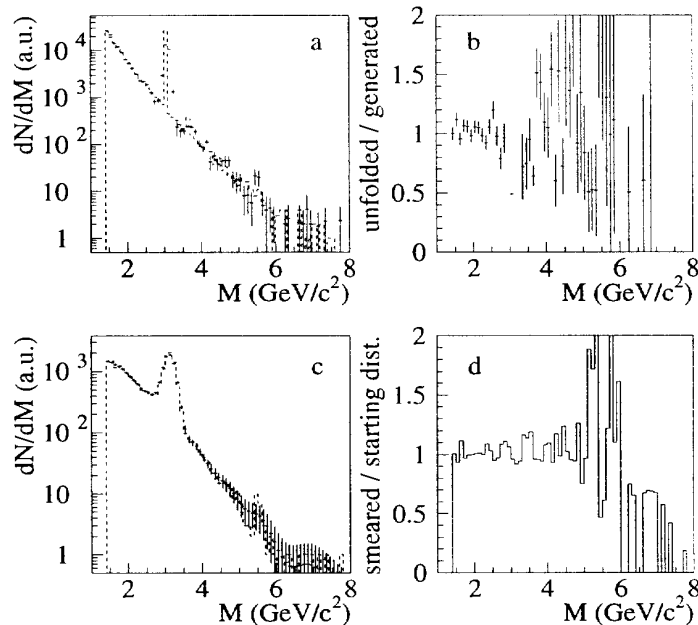

Fig. 8. Comparison (a) between unfolded (points) and Monte-Carlo generated (dashed lines) mass distributions together with their ratio (b). The distribution obtained by smearing the (unfolded) source mass spectrum is compared in (c) with the reconstructed starting distribution. Their ratio is shown in (d).

15

The analysis of mass and P_T spectra gives the results shown in Tables 6 and 7.

Table 6
Comparison between generated and unfolded mass distributions.

	Generated	Unfolded
DY Norm	113169	116315±5913
J/ψ Norm	26418	25995±389
ψ' Norm	195	169±70
J/ψ Width (MeV/c^2)	0	71±2
J/ψ Position (GeV/c^2)	3.097	3.089±0.002
ψ' Position (GeV/c^2)	3.685	3.76±0.05
DY Slope (GeV/c^2)	1.00	0.99±0.03

The corresponding unfolded mass and P_T distributions are shown in Fig. 9.

Table 7

Comparison between generated and unfolded P_T distribution moments: $< P_T >$ (GeV/c) and $< P_T^2 > $ (GeV/c)^2.

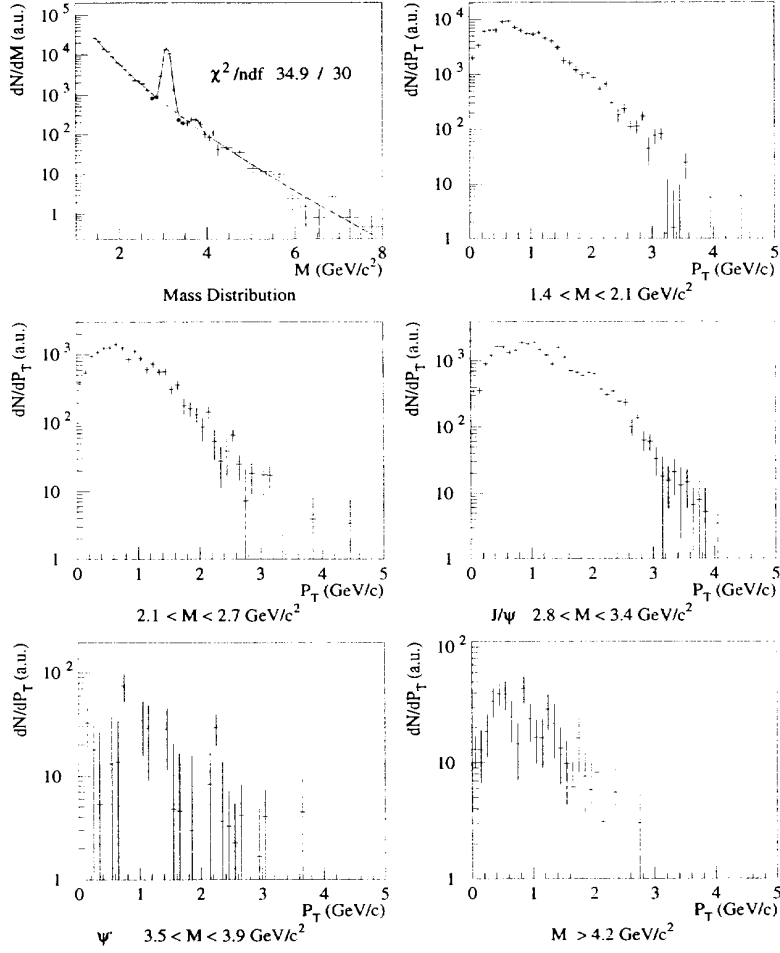| P_T	Generated		Unfolded	
	$< P_T >$	$< P_T^2 >$	$< P_T >$	$< P_T^2 >$
$2.1 \leq M \leq 2.7$ GeV/c^2	0.86	1.00	0.85 ± 0.03	1.01 ± 0.04
J/ψ	1.14	1.69	1.12 ± 0.02	1.65 ± 0.04
ψ'	1.21	1.92	1.13 ± 0.31	1.89 ± 0.57
$M > 4.2$ GeV/c^2	0.86	1.00	0.92 ± 0.10	1.15 ± 0.16

Fig. 9. Unfolded mass and P_T distributions (black dots correspond to points removed from the fit).

17

7 Unfolding of S-U data

The unfolding technique presented in the preceding paragraphs has been applied to the S-U data collected in 1992. Before presenting the results, one has to discuss two important points:

- when to stop the iterations,
- how to evaluate the uncertainties.

7.1 Convergence

The number of steps necessary to get the source distribution is not easy to determine. We have used a χ^2 comparison between successive unfolded distributions. The χ^2 value decreases continuously and does not saturate when the number of iterations increases. This technique does not seem very appropriate to determine the optimum number of iterations. Another criterion uses the fit of the J/ψ peak with a gaussian shape. The corresponding width has been plotted in Fig. 10 as a function of the iteration number. This figure shows that above 50 steps, the width decrease is negligible. From this figure alone, one can conclude that taking about 100 steps would be good enough. However, the shape of the deconvoluted spectra shows that the noise starts to increase when we use a high number of iterations. Therefore, we have decided to stop the iterations after 50 steps to avoid amplifying the fluctuations. We have checked that, above 50 steps, the different fitted parameters extracted from the mass and P_T spectra show a negligible variation with the number of iterations.

7.2 Error calculation

From formula (5), one can compute the error matrix, assuming that errors on smearing and acceptance matrices are negligible. However, the practical calculation of the 4-d error matrix involves computing matrices with 8 indices, leading to $\approx 10^{13}$ elements, which is completely out of reach. Thus, one has to find some realistic approximation. After several trials, it turns out that giving to each cell an error corresponding to the error of the data corrected only for acceptance, is a reasonable choice. This has been checked by computing a complete 1-d error matrix for the mass spectrum. Both error evaluation methods lead to similar values.
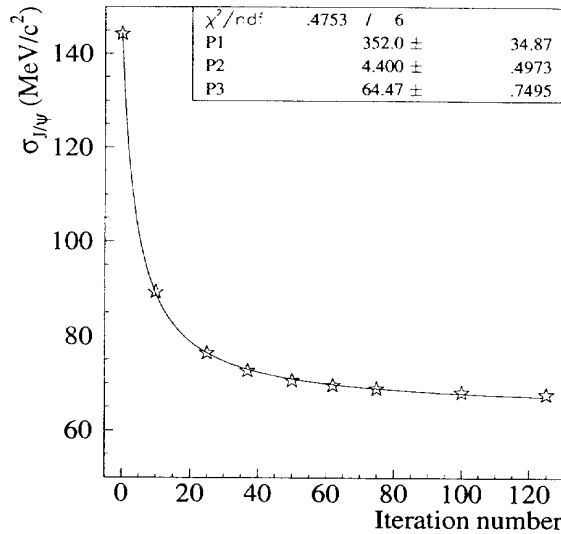
Fig. 10. Fitted width of the unfolded simulated J/ψ peak as a function of the iteration number. The solid line corresponds to a fit using the function: $\frac{P_1}{x+P_2} + P_3$.

7.3 Results

The resulting deconvoluted mass spectrum is shown in Fig. 11. After fitting the mass distribution with the same physical processes as considered in section 5, one can extract the P_T distributions (Fig. 11) and the $< P_T >$ and $< P_T^2 >$ values (Table 8) in different mass regions. These values are in agreement with those of Ref. [3].

Since the gaussian shapes used for the J/ψ and ψ' mass regions do not reproduce well the resonances, the numbers of J/ψ and ψ' have been extracted from the unfolded mass spectrum by subtracting the contribution of the fitted mass continuum in the corresponding mass intervals, that is $2.8 < M < 3.4$ GeV/c^2 for the J/ψ and $3.5 < M < 3.9$ GeV/c^2 for the ψ'. The resulting ratio ψ'/ψ is $(0.74 \pm 0.06)\%$, in agreement with Refs. [3,15].

8 Conclusion

We have described a method to unfold in a four-dimensional way the NA38 experimental data. We have used a non-linear iterative algorithm based on the method first proposed by Richardson and Lucy. This method has been shown to converge rapidly. The subtraction of the four-dimensional background requires special care and a technique has been proposed to avoid negative cell

19

Table 8

Unfolded P_T distribution moments $< P_T >$ $(\mathrm{GeV/c})$ and $< P_T^2 >$ $(\mathrm{GeV/c})^2$ in different mass intervals for S-U data.

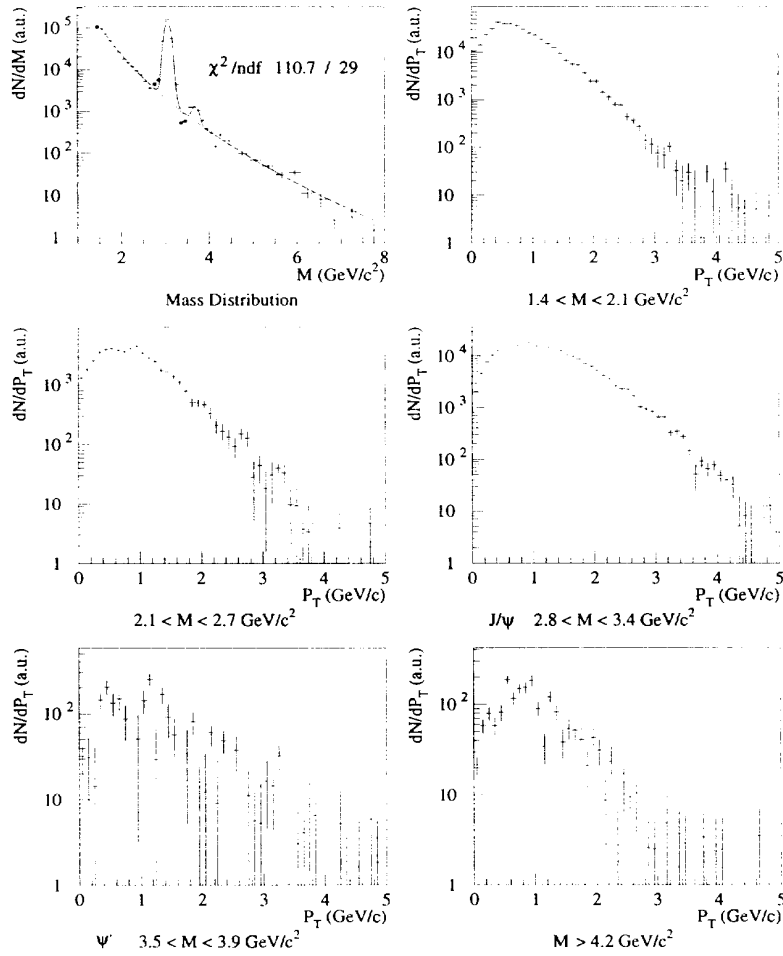|	$< P_T >$	$< P_T^2 >$
$2.1 < M < 2.7$ GeV/c^2	0.89 ± 0.02	1.07 ± 0.03
J/ψ	1.16 ± 0.01	1.75 ± 0.02
ψ'	1.21 ± 0.12	2.16 ± 0.29
$M > 4.2$ GeV/c^2	1.02 ± 0.05	1.44 ± 0.11

Fig. 11. Unfolded mass and P_T distributions for S-U data (black dots correspond to points removed from the fit).

20

contents. We have presented a practical approximation which allows to estimate the errors which cannot be exactly computed. Tests of the method have been shown in detail for the S-U experiment. It should be stressed that the main advantage of this multi-dimensional technique is to avoid any hypothesis concerning the shapes of the distributions in each variable and concerning the different physics processes which contribute to the measured spectra.

References

[1] NA38 Proposal, CERN/SPSC 85-20, SPSC/P 211;
NA50 Proposal, CERN/SPSLC 91-55, SPSLC/P 265-Rev.

[2] NA38 Collab., C. Baglin *et al.*, Phys. Lett. B251 (1990) 465;
NA38 Collab., C. Baglin *et al.*, Phys. Lett. B262 (1991) 362;
O. Drapier, Thesis, Université de Lyon, LYCEN T 9042 (1990).

[3] R. Mandry, Thesis, Université de Lyon, LYCEN T 9356 (1993).

[4] W.H. Richardson, J. Opt. Soc. Am. 62 (1972) 55.

[5] L.B. Lucy, A. J. 79 (1974) 745.

[6] L. Anderson *et al.*, NA10 Collaboration, Nucl. Instr. Meth. 223 (1984) 26.

[7] J.C. Collins and D.E. Soper, Phys. Rev. D16 (1977) 2219.

[8] Dimujet/Dimurec user's guides, NA38/NA50 internal notes.

[9] CERNLIB short writeup E105.

[10] A. Bodek and J.L. Ritchie, Phys. Rev. D23 (1981) 1070.

[11] J.G. Branson, Thesis, Princeton University (1977);
J. Badier, NA10 collaboration, internal note.

[12] G. D'Agostini, Nucl. Instr. Meth. A362 (1995) 487;
L. Lindemann and G. Zech, Nucl. Instr. Meth. A354 (1995) 516.

[13] L.B. Lucy, *The restoration of HST images and spectra II*, Space Telescope Science Institute, 1994, R.J. Hanisch and R.L. White, eds.

[14] S. Papillon, Thesis, Université Paris 7, IPNO T91-03 (1991);
S. Constantinescu, S. Dita and D. Jouan, IPNO DRE 96-01.

[15] A. Borhani, Thesis, Université Paris 6, (1996).